2019

Calculation of oxygen diffusion coefficients in oxide films formed on low-temperature annealed Zr alloys and their related corrosion behavior

Lina Zhang
Edith Cowan University

Liang-Yu Chen
Edith Cowan University, liangyu.chen@ecu.edu.au

Cuihua Zhao

Yujing Liu

Lai-Chang Zhang
Edith Cowan University, l.zhang@ecu.edu.au

10.3390/met9080850
Zhang, L., Chen, L. Y., Zhao, C., Liu, Y., & Zhang, L. (2019). Calculation of oxygen diffusion coefficients in oxide films formed on low-temperature annealed Zr alloys and their related corrosion behavior. *Metals*, *9*(8).

metals

MDPI

Article

Calculation of Oxygen Diffusion Coefficients in Oxide Films Formed on Low-Temperature Annealed Zr Alloys and Their Related Corrosion Behavior

Lina Zhang [1,2,3,4], Liang-Yu Chen [1,2,*], Cuihua Zhao [3], Yujing Liu [4] and Lai-Chang Zhang [2,*]

1 School of Science, Jiangsu University of Science and Technology, Zhenjiang 212003, China
2 School of Engineering, Edith Cowan University, 270 Joondalup Drive, Joondalup, Perth 6027, WA, Australia
3 Guangxi Key Laboratory of Processing for Non-ferrous Metals and Featured Materials, Nanning 530004, China
4 School of Mechanical and Chemical Engineering, The University of Western Australia, 35 Stirling Highway, Perth 6009, WA, Australia
* Correspondence: lychen@just.edu.cn (L.-Y.C.); lczhangimr@gmail.com or l.zhang@ecu.edu.au (L.-C.Z.); Tel.: +86-511-8440-1171 (L.-Y.C.); +61-8-6304-2322 (L.-C.Z.)

Received: 10 July 2019; Accepted: 31 July 2019; Published: 2 August 2019

Abstract: The growth of oxide film, which results from the inward oxygen diffusion from a corrosive environment, is a critical consideration for the corrosion resistance of zirconium alloys. This work calculates the oxygen diffusion coefficients in the oxide films formed on zirconium alloys annealed at 400~500 °C and investigates the related corrosion behavior. The annealed samples have a close size for the second-phase particles but a distinctive hardness, indicating the difference in substrate conditions. The weight gain of all samples highly follows parabolic laws. The weight gain of the sample annealed at 400 °C has the fastest increase rate at the very beginning of the corrosion test, but its oxide film has the slowest growth rate as the corrosion proceeds. By contrast, the sample annealed at 500 °C shows the lowest weight gain but the highest corrosion rate constant. Such a corrosion behavior is attributed to the amount of defects existing in the oxide film formed on the annealed samples; fewer defects would provide a lower fraction of short-circuit diffusion in total diffusion, resulting in a lower diffusion coefficient of oxygen in the oxide film, thereby producing better corrosion resistance. This is consistent with the calculated diffusion coefficients of oxygen in the oxide films: 3.252×10^{-11} cm^2/s, 3.464×10^{-11} cm^2/s and 3.740×10^{-11} cm^2/s for the samples annealed at 400 °C, 450 °C, and 500 °C, respectively.

Keywords: Zirconium alloy; corrosion; oxide; diffusion coefficient; annealing

1. Introduction

Zirconium (Zr) alloys are widely used as fuel claddings in nuclear reactors due to their adequate mechanical properties, low neutron absorption rate, and excellent corrosion resistance in service environments [1–4]. Among these properties, corrosion resistance is one of the most important considerations, as corrosion limits the service life of Zr alloys and is related to the safety of nuclear reactors [5–8]. When used in environments with high temperature and high pressure, Zr alloys react with H_2O (aqueous solution or steam) and are oxidized [6]. Therefore, dense oxide films are formed on the surface of Zr alloys [5,6]. These oxide films are protective and can reduce the ingression of oxidizing media (e.g., oxygen and/or other oxidizing species) [6]. Therefore, the corrosion rate is reduced while increasing the thickness of the oxide films formed on Zr alloys. When the thickness of the oxide films reaches 2~3 μm, a rapid increase in weight gain is noticed for Zr alloys [9–11]. Such a

phenomenon is always associated with the reduction in corrosion resistance of Zr alloys. Hence, much work has focused on the growth of oxide films formed on Zr alloys [5,12–14].

During service, the growth of oxide films formed on Zr alloys is determined by the inward diffusion of the oxidizing medium from the corrosive environments to the metal substrate [6,12,15]. It is well known that the formation and the growth of oxide films can be divided into several stages. According to the thermodynamics of the Zr–O system [16], oxygen is more stable when it dissolves in a Zr-rich phase compared to the formation of Zr–O oxides. The solubility of O in a Zr-rich phase at 300~400 °C is about 28.6 at.%. Therefore, oxygen would dissolve in the Zr metal phase before forming oxide films [15]. Once the concentration of O in a Zr-rich phase exceeds its solid solubility, an oxide film is formed. In this stage, the oxide films are only in a few monoatomic layers (~2 nm in thickness) [17]. These oxide layers are usually disordered and porous. Therefore, the growth of oxide film is significantly rapid since such an oxide film is non-protective [18]. Like the growth of oxide films, the corrosion rate of Zr alloy gradually decreases when the oxide films become protective. In general, the growth of an oxide film follows a parabolic or cubic law in this stage, which is also named a pre-transition stage. Therefore, it can be considered that the diffusion of oxygen is governed by the oxide films in the pre-transition stage [5]. After the pre-transition stage, a sharp increase in the corrosion rate of the Zr alloy can be observed. This phenomenon is called as transition in corrosion kinetics, which describes the beginning of the post-transition stage [19]. In this stage, the oxide films are split into two layers by long link-up cracks, and the outer layer of the oxide films is almost non-protective due to the existence of a large number of flaws (e.g., pores and cracks) [5]. As a result, the reduction in the thickness of the protective barrier (the inner layer of the oxide film) degrades the corrosion resistance of the Zr alloy. With the growth of the inner layer of oxide film, the corrosion rate decreases again, and, therefore, the corrosion kinetics of the alloy becomes periodic until the oxide film completely breaks down [20].

In previous work, alloy compositions have been stressed to influence the growth of oxide film in service environments [21,22]. For example, Lee et al. [21] found that the addition of Mo in Zr–1Nb–1Sn–0.1Fe alloy (in wt.%; the same hereafter) results in a lumpy feature on the surface of oxide films, and the modified alloy possesses a lower corrosion resistance than the Mo-free counterpart. Park et al. [22] pointed out that the oxides formed on a Zr–1.1Nb–0.05Cu alloy have a much larger grain size than those formed on Zr–1.5Nb–0.4Sn–0.2Fe–0.1Cr and Zr–1.3Sn–0.2Fe–0.1Cr alloys. Therefore, the Zr–1.1Nb–0.05Cu alloy has lower corrosion rate. Indeed, the production of Zr alloy fuel claddings should undergo several cycles of deformation and annealing. The Zr alloys with the same chemical compositions, but which experienced different processing procedures, can also exhibit distinctive corrosion resistance [6], which indicates the significant effect of substrate conditions on the growth behavior of oxide films. Different substrate conditions may lead to different characteristics of the formed oxide films, resulting in the distinguished diffusion behavior of oxygen through the oxide film, which also contributes to the distinction in growth of the oxide film. Unfortunately, few studies report on the oxygen diffusion coefficients in oxide films formed on Zr alloys with different substrate conditions. Therefore, it is highly significant to answer this open question, in order to underpin the corrosion behavior of Zr alloys in terms of the diffusion coefficients.

This work used a deformed Zr–Sn–Nb–Fe–Cu–O alloy sheet, which was finally annealed at different temperatures, elaborating the samples with different substrate conditions. After being corroded in an autoclave at 360 °C in an LiOH aqueous solution for 160 days, the corrosion kinetics of the samples were described in terms of their weight gain. As such, the oxygen diffusion coefficients in the oxide films and the adjacent substrates were calculated according to a suggested model. The calculated results illustrate the growth of the oxide film formed on the samples annealed at different temperatures, which advances the understanding of the corrosion behavior of Zr alloys.

2. Materials and Methods

2.1. Sample Preparation and Corrosion Test

A β-quenched Zr–Sn–Nb–Fe–Cu–O alloy sheet with a thickness of 10 mm was used as the experimental material. The nominal chemical compositions of this alloy were 0.55% Sn, 0.32% Fe, 0.35% Nb, 0.05% Cu, and 0.079% O, with Zr as the balance. The experimental alloy was hot rolled to 3 mm and annealed at 580 °C for 1 h. Then, the alloy was cold rolled to 1.8 mm and cut into three parts, which were finally annealed at 400 °C, 450 °C, and 500 °C for 5 h, respectively. The details of the processing procedure are shown in Figure 1. Like the other metallic materials [23–27], the excessive concentration of alloying elements beyond the solution solubility of Zr would lead to the formation of second-phase particles (SPPs), as frequently observed in various Zr alloys [28–30]. It has been also reported that SPPs can hardly grow during low-temperature annealing [31,32]. It is known that the recrystallization temperature of Zr alloys is about 480~500 °C, depending on their chemical compositions [33]. Therefore, the final annealing at 400~500 °C was selected for heat treatment in order to minimize the effect of SPPs on oxygen diffusion during corrosion tests.

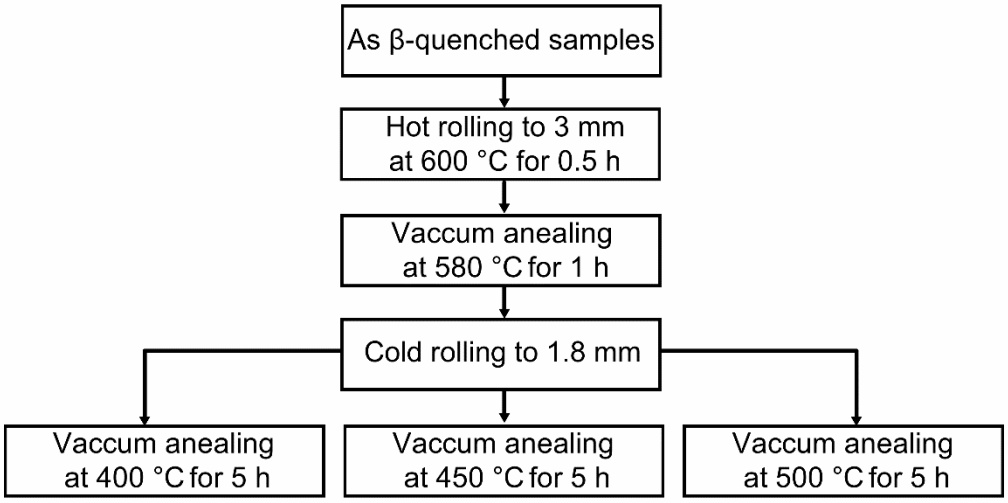

Figure 1. Processing flow of the experimental Zr alloy.

The final annealed samples were cut into 20 mm × 15 mm × 1.8 mm in dimension and chemically polished in a mixed solution composed of H_2O, HNO_3, H_2SO_4, and HF (3:3:3:1 in vol.%). All reagents mentioned in the current work were produced by Sinopharm Chemical Reagent Co., Ltd. (Beijing, China). Corrosion tests were carried out via immersion in a 0.01 M LiOH aqueous solution at 360 °C (i.e., 633 K) under a saturation pressure of 18.6 MPa in an isothermal static autoclave in terms of ASTM-G2/88. The weight gain of the samples was measured according to the ratio of weight augmentation and the total surface area of the sample. Corrosion immersion tests were conducted for up to 160 days. For easy description, the samples were denoted by the final annealing temperature and exposure time. For example, FA-400 was for the sample that was finally annealed at 400 °C, and FA-400-3 indicated the FA-400 sample after immersion for 3 days, and so on.

2.2. Characterizations

The samples for microstructural observations were prepared by standard metallographic procedures and then etched in a mixed solution composed of H_2O, HNO_3, and HF (9:9:2 in vol.%) for about 15 s. The microstructures of the etched samples (along the rolling direction–transverse direction planes) were characterized by an FEI Quanta 250 field emission gun scanning electron microscope (SEM, FEI, Hillsboro, TX, USA). At least, 8 SEM images, at a magnification of 50,000, were used to obtain the statistical information of the SPPs, using the Image-Pro Plus 5.0 software (Media Cybernetics,

Rockville, MD, USA). Hardness tests were conducted on the etched samples by using an automatic hardness tester. The load for indentation was 5 N, with a dwell time of 15 s. Ten individual tested points were tested for each sample to obtain the average value. The phase constituents of the oxide films formed on the samples at different exposure times were examined by grazing incidence X-ray diffraction (GIXRD). The grazing incidence angle was 2°, with the aim to reduce the contribution from the substrate. The XRD data were analyzed by Jade 6.5 (Materials Data Inc., Livermore, CA, USA).

2.3. Model and Calculation Method

Usually, the corrosion (oxidation) takes place on the surface of Zr alloys in a high-temperature aqueous environment [34]. Therefore, it is believed that the corrosion of Zr alloys results from the diffusion of oxygen in oxide films toward the substrate. Since oxide films have a considerable number of oxygen vacancies, oxygen ions become the main diffusing species, resulting from the reaction of $V_O + 2e^- + H_2O \rightarrow O^{2-} + H_2\uparrow$ (V_O is oxygen vacancy) [35,36]. On the other hand, the dissolution of the oxide films would influence the diffusion of oxygen [37]. However, the oxide films formed on Zr alloys are significantly stable in the corrosive environment used in this work and can hardly dissolve in a corrosive medium [35,38]. Therefore, the dissolution of the oxide film was not considered in this work. Based on the above considerations, several assumptions were used to build a reasonable model.

(i) The diffusion of oxygen in the oxide film occurs via the vacancy mechanism;
(ii) The diffusion coefficients of oxygen in the oxide and substrate are constant;
(iii) The increase in the weight gain of the sample only results from the absorption of oxygen;
(iv) No electric field or local space charge exists in the oxide film;
(v) No sub-oxide is present between the oxide film and the substrate;
(vi) No dissolution of the oxide film is considered.

Therefore, a two-phase model, suggested in the literature, was used to illustrate the concentration of oxygen in oxide films and in the adjacent substrate [39,40]. In this model (Figure 2), the concentration of oxygen was assumed to follow a parabolic law, since the diffusion of the element meets the Arrhenius equation for the given temperatures and metallic materials [41–43]. As represented in Figure 2, the x axis indicates the distance from the oxide surface; x_0 is the oxide surface and x_1 is the oxide/substrate interface. As the corrosion proceeds, the oxide/substrate interface (x_1) moves towards the substrate, thickening the oxide films. The y axis is the concentration of oxygen in the oxide film and the substrate. C_1 is the oxygen concentration at the oxide/environment interface, which equals 1.526 g/cm^3 [35]. C_2 is the concentration of oxygen at the oxide/substrate interface (oxide side). The concentration's value is $1.5494–9.7 \times 10^{-4}$ T g/cm^3 [35], where T is the absolute temperature in K. Because T was 633 K in this work, C_2 is equal to 1.486 g/cm^3. C_3 is the concentration of oxygen at the oxide/substrate interface (substrate side) and can be regarded as the saturation concentration of oxygen in α-Zr. For the Zr–O phase diagram [16], C_3 was calculated to be 0.459 g/cm^3.

To calculate the diffusion coefficient of oxygen in the oxide films and the substrate, the Fick's second law equation for diffusion from a constant source into a semi-infinite medium was employed [35]. The equation used is shown below:

$$C(x,t) = A + B \cdot \mathrm{erf}\left(\frac{x}{2\sqrt{Dt}}\right) \quad (1)$$

where $C(x,t)$ is the concentration of oxygen in the oxide films or the substrate; A and B are constant; erf is the error function; x is the diffusion length for oxygen; t is time; and D is the diffusion coefficient of oxygen.

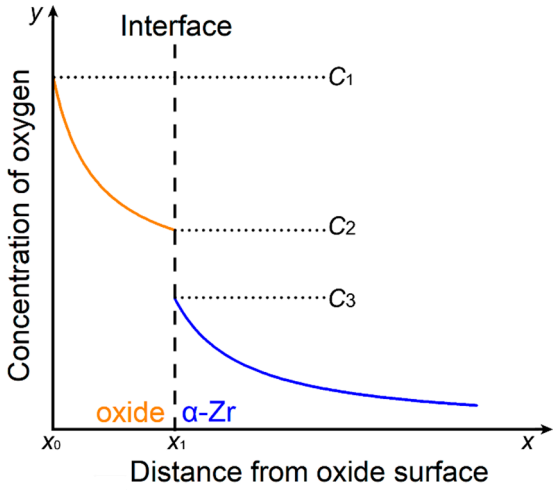

Figure 2. Schematic illustration of the oxygen concentration in the oxide film and the substrate by a suggested model (Reproduced form reference [39], with permission of Elsevier).

3. Results and Discussion

3.1. Characterizations of the Substrates

Figure 3 shows the SEM images for the microstructures of the alloy samples and the statistical information of the SPPs. As seen in Figure 3a–c, all samples have a similar microstructure. Numerous tiny SPPs (as indicated by hollow arrows) are uniformly distributed in the matrix. The average diameters of SPPs for FA-400, FA-450, and FA-500 are revealed in Figure 3d. The SPPs in FA-400 have an average diameter of 40 nm (Figure 3d). Although heat treatment can enhance the growth of SPPs in Zr alloys [28,44], the average diameter of SPPs in FA-450 (41 nm) is almost the same as that in FA-400. The FA-500 has a slightly larger average diameter for SPPs (43 nm) than FA-400 and FA-450. However, compared with the SPPs in some Zr alloys (ranging from 50~100 nm in average diameter), the SPPs in the samples used in this work are significantly small and have no apparent distinction, which is attributed to their relatively low temperature in the final annealing treatment [28,44]. Chai et al. [28] pointed out that the SPPs in the Nb-containing Zr alloys have a larger coarsening activation energy than those in the Nb-free Zr alloys. Therefore, it is reasonable that no obvious distinction in the size of SPPs is observed in the samples annealed at at 400~500 °C.

The hardness of FA-400, FA-450, and FA-500 continuously decreases while increasing the annealing temperature (Figure 4). FA-400 has the highest hardness of 241 HV, which is greater than the hardness of FA-450 and FA-500 (233 HV and 222 HV, respectively). It is well known that defects (such as dislocations or boundaries) can be induced in the alloys after deformation [45–47]. Such defects enhance the hardness and strength of the alloys and can be healed by heat treatment [48–50]. Yang et al. [51] suggested that the strengthening effect of SPPs in Zr alloys during heat treatment is often minimal. Therefore, variation in the hardness of the samples should be attributed to a change in the Zr matrix. Since the melting point temperature (T_m) of Zr is 1855 °C (2128 K), the recovery temperature and recrystallization temperature of Zr can be calculated to be $0.35T_m$ of 472 °C (745 K) and $0.4T_m$ of 578 °C (851 K), respectively [29]. As such, the final annealing temperature of 400 °C is significantly lower than the recovery temperature. In comparison, 450 °C is slightly lower than the recovery temperature while 500 °C is somewhat higher than the recovery temperature but significantly lower than the recrystallization temperature. Due to recovery, the defects induced by cold rolling would disappear during the final annealing [49]. Apparently, the sample with the lower final annealing temperature would have a larger number of defects. As a result, different processing procedures lead to different substrate conditions for the samples.

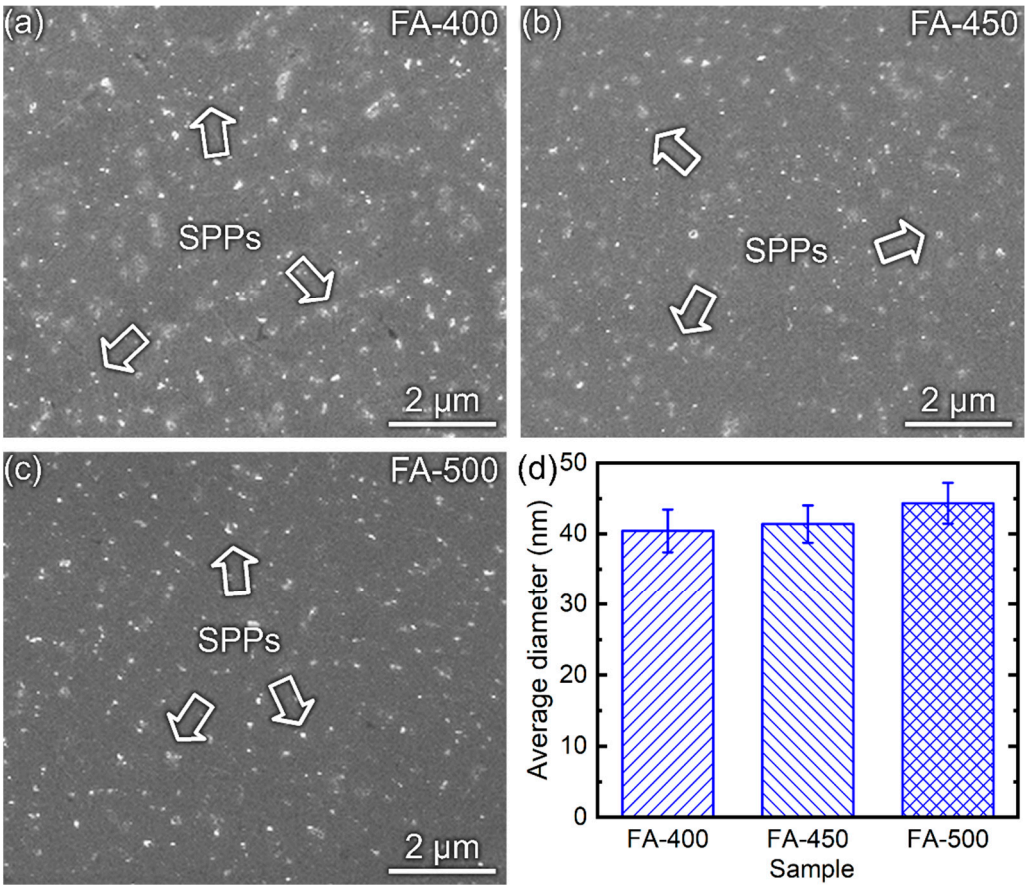

Figure 3. The SEM images for the microstructures of the alloy samples: (**a**) FA-400, (**b**) FA-450 and (**c**) FA-500, and (**d**) the corresponding statistical information of the second-phase particles (SPPs).

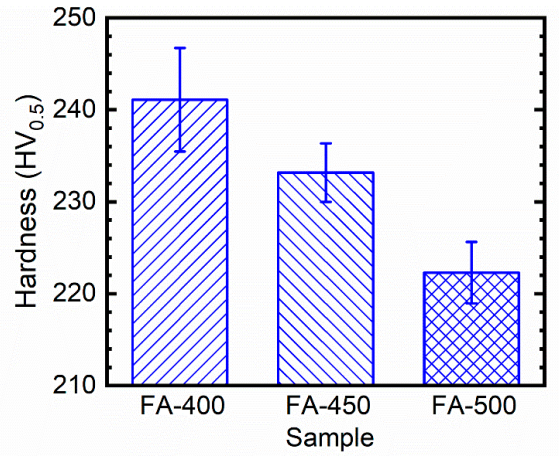

Figure 4. Hardness of the samples after final annealing.

3.2. Corrosion Kinetics and the Phase Constituents of the Corroded Samples

Figure 5 reveals the weight gain versus the exposure time in the immersion tests for all samples. It is clearly found that the weight gain curves of all samples obey parabolic laws. At the early stage of the corrosion test, the weight gain of the samples increases rapidly. It can be understood that oxygen can easily ingress into the samples since the oxide films formed on Zr alloys have low protectiveness in this stage [18]. The weight gain of Zr alloys is ascribed to the inward diffusion of oxygen into the substrate from corrosive environments to the metal substrate. Because the oxygen diffusion coefficient

in the oxide film is significantly lower than that in the Zr-rich phase, a decreased corrosion rate is observed as the corrosion test proceeds. Therefore, it can be considered that the increase in the weight gain of the samples is governed by the diffusion of oxygen in the oxide films [5]. With up to a 160-day exposure, no transition in corrosion kinetics is observed (Figure 5), indicating that all samples are still in the pre-transition stage. Interestingly, the difference in the weight gain for all samples becomes less by increasing the exposure time. This result illustrates that the oxide films formed on different samples have different growth behaviors.

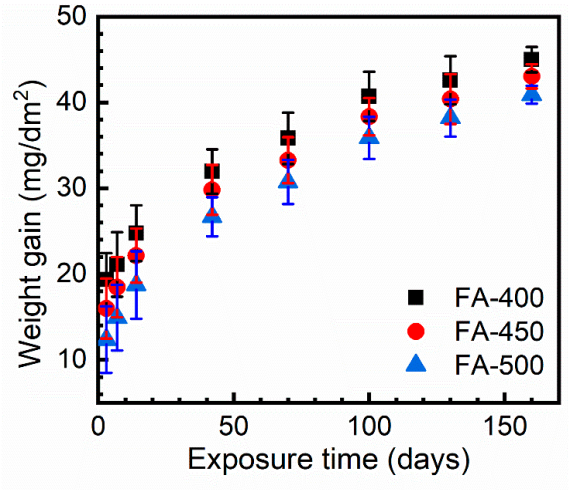

Figure 5. Weight gain versus exposure time for all samples.

Figure 6 shows the GIXRD results of the corroded samples after 3-day and 42-day exposures. It can be seen that the oxide film mainly consists of monoclinic zirconia (m-ZrO_2), which is consistent with the results in [5,52,53]. Due to the contribution of the substrate, the diffraction peaks of α-Zr can still be observed on the GIXRD patterns for all samples corroded after a 3-day exposure (Figure 6a). By contrast, the intensities of the peaks of α-Zr become much weaker in the GIXRD patterns for all samples after a 42-day exposure (Figure 6b). Such phenomena indicate an increase in the thickness of the oxide film (and the decreased contribution of the substrate for GIXRD as well). However, the peaks of m-ZrO_2 still dominate. Therefore, using a two-phase model to calculate the diffusion coefficients of oxygen is reasonable in this work.

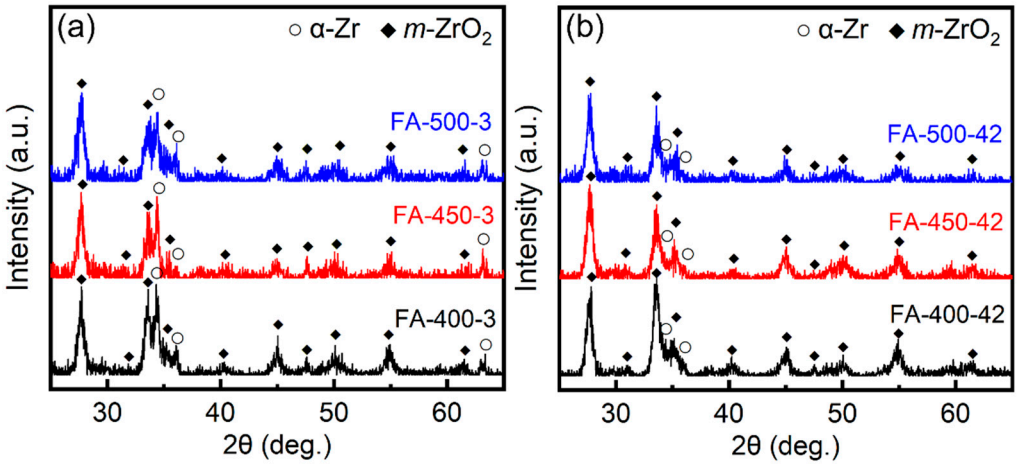

Figure 6. Grazing incidence X-ray diffraction (GIXRD) patterns for the FA-400, FA-450, and FA-500 immersed with (**a**) 3-day and (**b**) 42-day exposure.

As the weight gain of Zr alloys approximately obeys a parabolic law, corrosion kinetics can be evaluated by following equation [6]:

$$w = kt^n \tag{2}$$

where w is the weight gain, k is a constant, t is exposure time, and n is corrosion rate constant. Taking a logarithm of both hands of Equation (2) yields

$$\ln w = \ln k + n \ln t. \tag{3}$$

Inputting the values of w and t obtained in the corrosion test (Figure 5) into Equation (3), one can obtain the values of $\ln k$ and n for different samples by linear fitting, as plotted in Figure 7. The fitting results are listed in Table 1. Apparently, the slopes of n are significantly different, indicating that the three samples have distinctive corrosion rates. For a parabolic curve, the exponential n illustrates the gradient of the function value at a given base number. FA-400 has the smallest n of 0.222 compared with the other two samples (0.256 and 0.308 for FA-450 and FA-500, respectively), illustrating that the oxide film formed on FA-400 has the lowest growth rate among the three samples during the corrosion test. However, these three samples show significantly different $\ln k$ values. $\ln k$ is the intercept, specifying the weight gain of the samples when t equals 1. Hence, $\ln k$ can also be used to elucidate the initial weight gain of the samples in the very beginning of the corrosion test. FA-400 has the largest value of $\ln k$ among the three samples, indicating that the growth rate of the oxide film formed on FA-400 is the highest in the very beginning of the corrosion test but becomes the lowest as the corrosion processes. By contrast, the weight gain of FA-500 is the lowest after a 3-day exposure. Nevertheless, the oxide film formed on FA-500 grows faster than the film formed on the other two counterparts. Therefore, combining the mechanism for the formation and growth of oxide films formed on Zr alloys [6,12,15], one can conclude that the diffusion coefficients of oxygen should be different in the oxide films formed on the samples.

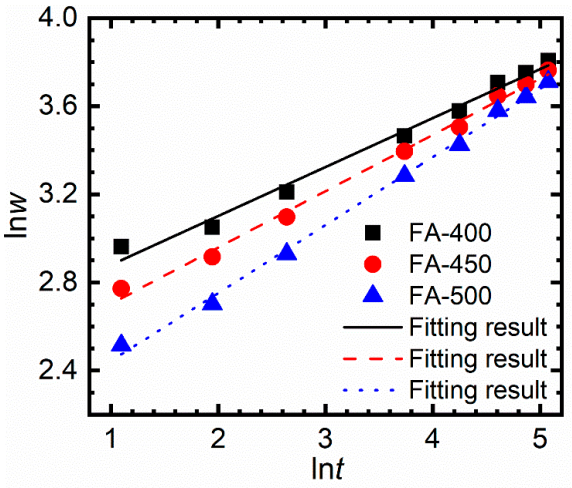

Figure 7. Fitting results of the corrosion kinetics for FA-400, FA-450, and FA-500.

Table 1. Results of $\ln k$, n, and k by using the data of weight gain for the three samples.

Constant	FA-400	FA-450	FA-500
n	0.222	0.256	0.308
$\ln k$	2.656	2.447	2.134
k (mg/dm^2)/day^n	14.240	11.554	8.449

3.3. Diffusion Coefficient of Oxygen in Oxide Film

According to Figure 2, the source with a constant oxygen concentration is located at the surface of the sample (x_0). As such, the thickness of the oxide film (d) can be expressed as the difference between the surface of the sample and the position of the oxide/substrate:

$$d = x_1 - x_0. \tag{4}$$

It is well known that the thickness of oxide film increases parabolically with time before the transition in corrosion kinetics [54]. According to Equation (2), Equation (4) can also be expressed as:

$$d = k_d t^n \tag{5}$$

where k_d is a constant for the growth of oxide film. The average thickness of the oxide films formed on FA400, FA-450, and FA-500 after a 160-day exposure (examined by SEM) is about 2.94 μm, 2.82 μm, and 2.68 μm, respectively. Therefore, k_d can be approximately calculated according to the fitting result of n in Table 1. The calculated values of k_d for FA400, FA-450, and FA-500 are 0.953, 0.769, and 0.561, respectively. If there is still no oxide film formed (before corrosion test), $x = 0$ is the initial position of the substrate surface. Hence, the x_1 can be defined as

$$x_1 = d/P \tag{6}$$

where P is the Pilling-Bedworth ratio for Zr–ZrO_2 system and approximately equal to 1.56 [55]. The Pilling–Bedworth ratio indicates the volume change before and after the oxidation of Zr. Parise et al. [56] reported that anisotropic volume dilatation takes place during the oxidation of Zr, which is approximately 0.005:0.54 in the parallel/perpendicular direction to the oxide/substrate interface. For a such a small ratio, the dilation of the oxide film in a parallel direction to the oxide/substrate interface can be neglected in this work. Hence, the volume change in the oxidation of the substrate fully contributes to the growth of the oxide film in a perpendicular direction to the oxide/substrate interface. Therefore, Equation (6) is valid.

As such, the diffusion coefficient of oxygen in the oxide film can be determined by Equation (7):

$$C_f(x,t) = A_f + B_f \cdot \mathrm{erf}\left(\frac{x - x_0}{2\sqrt{D_f t}}\right) \tag{7}$$

where $C_f(x,t)$ is the oxygen concentration in the oxide film, D_f is the diffusion coefficient of oxygen in the oxide film, and A_f and B_f are the constant.

In terms of the model shown in Figure 2, the boundary conditions for Equation (7) can be expressed by Equations (8) and (9):

$$C_f(x,t) = C_1 \text{ for } x = x_0,\ t > 0, \tag{8}$$

$$C_f(x,t) = C_2 \text{ for } x = x_1,\ t > 0. \tag{9}$$

From Equations (8) and (9), it can be understood that:

$$A_f = C_1 \tag{10}$$

$$B_f = \frac{C_2 - C_1}{\mathrm{erf}\left(\frac{d}{2\sqrt{D_f t}}\right)}. \tag{11}$$

Therefore, the oxygen flux at the surface of the oxide film (x_0) can be expressed as

$$J_{(x_0)} = -D_f \frac{\partial C_f(x,t)}{\partial x}. \tag{12}$$

Since the increase in the weight gain of the sample only results from the absorption of oxygen, the oxygen flux at x_0 can also be represented as

$$J_{(x_0)} = \frac{dw}{dt}. \tag{13}$$

Hence

$$-D_f \frac{\partial C_f(x,t)}{\partial x} = -D_f \frac{C_2 - C_1}{erf\left(\frac{d}{2\sqrt{D_f t}}\right)} \cdot \frac{2}{\sqrt{\pi}} exp\left[-\left(\frac{x - x_0}{2\sqrt{D_f t}}\right)^2\right] \cdot \frac{1}{2\sqrt{D_f t}}, \tag{14}$$

$$\frac{dw}{dt} = knt^{n-1}. \tag{15}$$

Let

$$C_1 - C_2 = \Delta C \tag{16}$$

$$\beta = \frac{d}{2\sqrt{D_f t}}. \tag{17}$$

Combining Equations (14) and (15) yields

$$\frac{\Delta C k_d}{2nk} = \beta \sqrt{\pi} erf(\beta). \tag{18}$$

Since D_f is a function of β, the diffusion coefficient of oxygen in the oxide film can be determined by the exact solution of Equation (18). The D_f results are listed in Table 2. Apparently, the diffusion coefficients of oxygen, which increase by increasing the temperature of annealing, are not identical in the different oxide films.

Table 2. Calculated diffusion coefficients of oxygen in the oxide films obtained by Equation (18).

Diffusion Coefficient	FA-400	FA-450	FA-500
D_f (cm^2/s)	3.252×10^{-11}	3.464×10^{-11}	3.740×10^{-11}

3.4. Diffusion Coefficient of Oxygen in a Substrate

The calculation of the diffusion coefficient of oxygen in the substrate (α-Zr) is helpful for specifying the growth of the oxide film formed on the samples. It should be noted that the weight gain of the sample is the sum of the oxygen in the oxide film and substrate. Therefore, the diffusion coefficient of the oxygen in the substrate can be evaluated using the weight gain of the sample and the corresponding thickness of the oxide film. According to Figure 2, Equation (1) can be rewritten as

$$C_s(x,t) = A_s + B_s \cdot \text{erf}\left(\frac{x}{2\sqrt{D_s t}}\right) \tag{19}$$

where $C_s(x,t)$ is the oxygen concentration in the substrate, D_s is the oxygen diffusion coefficient in the substrate, and A_s and B_s are the constants.

In terms of boundary conditions, $C_s(x,t)$ can be expressed as

$$C_s(x,t) = C_3 \text{ for } x = x_1,\ t > 0 \tag{20}$$

$$C_s(x,t) = C_0 \text{ for } x = \infty,\ t > 0 \tag{21}$$

where C_0 is the initial oxygen concentration in the substrate and approximately equal to 0.005 g/cm^3. From Equations (20) and (21), it can be known that

$$A_s = \frac{C_0 - C_3 \mathrm{erf}(\frac{k_d t^n}{2P\sqrt{D_s t}})}{1 - \mathrm{erf}(\frac{k_d t^n}{2P\sqrt{D_s t}})} \tag{22}$$

$$B_s = \frac{C_0 - C_3}{1 - \mathrm{erf}(\frac{k_d t^n}{2P\sqrt{D_s t}})}. \tag{23}$$

As mentioned above, the weight gain of the sample can be divided into two parts:

$$w = m_1 + m_2 \tag{24}$$

where m_1 is the mass of the oxygen in the oxide film and m_2 is the mass of the oxygen in the substrate. Therefore, these two variants can be expressed as:

$$m_1 = \int_{x_0}^{x_1} C_f(x,t)dx. \tag{25}$$

Due to the complexity of the integration of Equation (25), an approximate method, which describes a linear concentration distribution of oxygen in the oxide film, is adopted:

$$m_1 = x_1 \cdot \left(\frac{C_1 + C_2}{2}\right). \tag{26}$$

m_2 can be calculated by the difference in the total weight gain of the sample and the mass of the oxygen in the oxide film (m_1), which is also equal to the integration of the oxygen flux at the oxide/substrate interface in the time range from 0 to t. Therefore, m_2 can be expressed as:

$$m_2 = w - m_1 = \int_0^t J(x_1,t)dt \tag{27}$$

where $J(\mathrm{x}_1,t)$ is the oxygen flux at the oxide/substrate interface. Then, differentiating Equation (27) and considering (2), (5), and (26) yield:

$$J(\mathrm{x}_1,t) = knt^{n-1} - \frac{(C_1 + C_2)}{2} k_d n t^{n-1}. \tag{28}$$

Due to the fixed concentration of the oxygen at the oxide/substrate interface (on the substrate side), the oxygen flux at $x = x_1$ can be expressed as:

$$J(\mathrm{x}_1,t) = -D_s \frac{\partial C_s(x,t)}{\partial x} = \frac{C_3 - C_0}{1 - erf\left(\frac{k_d t^n}{2P\sqrt{D_s t}}\right)} \cdot \frac{1}{\sqrt{\pi}} \exp\left[-\left(\frac{\frac{d}{\mathrm{P}}}{\sqrt{D_s t}}\right)^2\right] \cdot \sqrt{\frac{D_s}{t}}. \tag{29}$$

Then, combining Equations (28) and (29) gives

$$knt^{n-1} - \frac{(C_1 + C_2)}{2} \frac{k_d n t^{n-1}}{\mathrm{P}} = \frac{C_3 - C_0}{1 - erf\left(\frac{k_d t^n}{2P\sqrt{D_s t}}\right)} \cdot \frac{1}{\sqrt{\pi}} \exp\left[-\left(\frac{\frac{d}{\mathrm{P}}}{\sqrt{D_s t}}\right)^2\right] \cdot \sqrt{\frac{D_s}{t}}. \tag{30}$$

The diffusion coefficient of oxygen in the substrate can be calculated by the exact solution of Equation (30). The results are listed in Table 3. One can note that the diffusion coefficient of oxygen in the FA-400 (5.472×10^{-11} cm^2/s) is smaller than that in the FA-450 and FA-500 (6.862×10^{-11} cm^2/s and

8.993×10^{-11} cm^2/s for the FA-450 and FA-500, respectively). Among these three samples, the corrosion rate of FA-400 becomes the slowest during corrosion (Figures 5 and 7). Therefore, the results of the diffusion coefficient of oxygen in the substrate are consistent with the corrosion kinetics of these three samples. One should note that the diffusion coefficients of oxygen in the substrates listed in Table 3 are calculated after the formation of the oxide film and based on the oxygen flux at the oxide/substrate interface. These values demonstrate that the corrosion rates of the samples are governed by D_f after the protective oxide film is formed. Therefore, these values should not be considered as the intrinsic diffusion coefficients of oxygen in the substrate at 360 °C.

Table 3. Calculated diffusion coefficients of oxygen in the substrate obtained by Equation (30).

Diffusion Coefficient	FA-400	FA-450	FA-500
D_s (cm^2/s)	5.472×10^{-11}	6.862×10^{-11}	8.993×10^{-11}

3.5. Oxide Growth of the Low-Temperature Annealed Samples

Oxygen's diffusion into the substrate is important to the growth of the oxide formed on the samples, since α-Zr has a maximum solubility of 28.6 at.% for oxygen at 300~400 °C [16]. If the concentration of oxygen exceeds 28.6 at.%, new oxides would be formed at the oxide/substrate interface. In this work, all samples reveal a significantly distinctive hardness after cold work followed by low-temperature annealing. One can understand that the deformation generally induces defects (such as boundaries and dislocations) to the metallic materials, and such defects can be healed by heat treatment [57–59]. In terms of the temperature adopted in heat treatment, recovery takes place in the heat-treated metallic materials [60,61]. The samples heat-treated at different temperatures result in a distinguished number of defects in the microstructure and, therefore, show significantly different hardness. Substantially, these findings elucidate that the FA-400, FA-450, and FA-500 samples have different substrate conditions.

It is known that defects play a role in the shortcuts for the mass transfer in many materials [62–65]. Panicaud et al. [66] pointed out that short-circuit diffusion exists in the nanocrystallization treated Zr alloys. Chen et al. [4] found that the degree of deformation can significantly influence the mass transfer of the second-phase particles in the Zr alloys. Therefore, different diffusion coefficients can be found in materials with the same chemical compositions but distinctive processing procedures. According to Figure 5, the weight gain of FA-400 has the fastest increase rate in the initial of the corrosion tests, illustrating that oxygen can easily diffuse into FA-400 at this stage. As mentioned above, oxide film forms after the concentration of oxygen exceeds its maximum solubility in α-Zr. Hence, the diffusion coefficients of the oxygen in the substrate govern the weight gain of the samples before the formation of the oxide film. FA-400 has the highest hardness and, therefore, is speculated to have the largest number of defects. As such, oxygen is prone to diffuse into FA-400 at a very early stage in the corrosion test. Correspondingly, FA-400 possesses the highest weight gain after a 3-day exposure.

Wang et al. [13,67] reported that only nanosized zirconia grains form on the surface of Zircaloy-4 after a short-time corrosion. Gong et al. [52] also observed this phenomenon and pointed out that the nanosized zirconia grains formed on the surface of Zircaloy-4 are almost defenseless against the ingression of oxygen in the corrosive environment. Therefore, the corrosion rates of the samples are still relatively fast at the early stage of corrosion. However, as the corrosion progresses, the corrosion rates of all samples decrease (Figure 5). In such a situation, the corrosion rate of the sample is governed by the diffusion coefficient of the oxygen in the oxide film. The fitting results in Table 1 show that the weight gain of the samples highly obeys parabolic laws (Equation (2)). From the view of mathematics, exponent n indicates the increment by increasing the exposure time t in Equation (2). The value of n for FA-400 (0.222) is lower than the value of FA-450 and FA-500 (0.256 and 0.308 for FA-450 and FA-500, respectively). Such a result demonstrates that a decrease in the corrosion rate of FA-400 is more significant than a decrease in the other two samples. This also indicates that the oxide growth

rate of FA-400 is the lowest among the three samples, which is consistent with the calculated diffusion coefficient of oxygen in the oxide film (Table 2).

In the previous works, an effective diffusion coefficient of oxygen for the suggested materials is proposed as follows [4,68]:

$$D_e = fD_d + (1 - f)D_l \tag{31}$$

where D_e stands for the effective diffusion coefficient (equal to D_f), D_d is the short-circuit (such as grain boundary and dislocation) diffusion coefficient, D_l indicates the lattice diffusion coefficient, and f is the proportional coefficient for D_d and D_l in the materials. Both D_d and D_l are temperature-dependent—i.e., D_d and D_l are fixed values for a specific material at a given temperature. Generally, D_d is significantly higher than D_l [68]. In this work, the calculated diffusion coefficient of oxygen in the oxide film for FA-400 (3.252×10^{-11} cm^2/s) is lower than that for FA-450 and FA-500 (3.464×10^{-11} cm^2/s and 3.740×10^{-11} cm^2/s respectively for FA-450 and FA-500). Based on the definition of the effective diffusion coefficient, it is speculated that fewer shortcuts exist in the oxide film formed on FA-400 compared to the oxide film formed on FA-450 and FA-500. Therefore, according to the continuation of the corrosion, the decrease in the corrosion rate of FA-400 is more apparent than that of FA-450 and FA-500.

Interestingly, the different values of D_f elucidate the distinctions in the oxide films formed on the samples annealed at different temperatures. The deformed sample annealed at the lowest temperature shows the fastest increase in weight gain at the very initial stage of corrosion. However, the D_f is the lowest in the oxide film formed on this sample. Defects may influence the growth of the oxide formed on the sample. Ly et al. [69] found that the Zr alloys with more grain boundaries have lower residual loop-stress accumulation, thereby demonstrating better corrosion resistance compared to the counterpart with fewer grain boundaries. Chen et al. [6] also pointed out that the oxide film formed on the 470 °C, the annealed Zr alloys show fewer micro cracks-compared to their counterpart formed on 570 °C annealed Zr alloys. Liu et al. [70] illustrated that the oxide film formed on 470 °C annealed Zr alloys is more compact and has fewer flaws than that formed on 520 °C annealed Zr alloys using nano-indentation tests. This work calculates the corrosion kinetics of Zr alloys and the diffusion coefficients of oxygen in their oxide films, and the results indicate that different substrate conditions substantially influence the growth of the oxide film formed on Zr alloys. Such a distinction can further determine the corrosion resistance of Zr alloys. However, the mechanism for the nucleation and growth of the oxide grains coupling the defects is still unclear. For instance, the cold-worked Zr alloys exhibit inferior corrosion resistance, whereas low-temperature annealed Zr alloys show better corrosion resistance [69,71]. This result indicates that excessive defects in Zr alloys may not help to improve their corrosion resistance. Therefore, more dedicated work on this topic is still needed in the future.

4. Conclusions

In the present work, a deformed Zr–Sn–Nb–Fe–Cu–O alloy was annealed at 400 °C, 450 °C, and 500 °C, respectively (denoted as FA-400, FA-450, and FA-500, respectively). The microstructures and hardness of the alloy samples were characterized. Afterwards, the corrosion behavior of the alloy samples was investigated. According to a suggested model and the weight gain of the alloy samples, the diffusion coefficients of oxygen in the oxide film and the substrate were calculated. Some key conclusions are drawn as follows:

(1) All alloy samples have similar microstructures, with numerous uniformly distributed tiny second-phase particles (SPPs). The average diameters of SPPs (40~43 nm) are almost identical in FA-400, FA-450, and FA-500. However, FA-400 has the highest hardness of 241 HV, which is greater than FA-450 and FA-500 (233 HV and 222 HV, respectively).

(2) The alloy samples are corroded in an autoclave in LiOH aqueous solution at 360 °C for up to 160 days. The weight gain of the samples closely follows the parabolic law of $w = kt^n$. The fitting results show that the values of n are 0.222, 0.256, and 0.308 for FA-400, FA-450, and FA-500, respectively.

By contrast, the values of k are 14.240, 11.554, and 8.449 for FA-400, FA-450, and FA-500, respectively, which shows a reversed order compared to the values of n. Such results indicate that the weight gain of FA-400 increases fastest at the very initial stage of the corrosion test, but the oxide film grows slowest as the corrosion progresses.

(3) Based on a suggested two-phase model and weight gain of the samples, the diffusion coefficients of oxygen in the oxide films are calculated to be 3.252×10^{-11} cm^2/s, 3.464×10^{-11} cm^2/s, and 3.740×10^{-11} cm^2/s for FA-400, FA-450, and FA-500, respectively, which is consistent with the fitting results of corrosion kinetics. The diffusion coefficients of oxygen in the substrate are lower than the diffusion coefficients of oxygen in the oxide films, which are calculated to be 5.472×10^{-11} cm^2/s, 6.862×10^{-11} cm^2/s, and 8.993×10^{-11} cm^2/s for FA-400, FA-450, and FA-500, indicating that the growth of oxide film is governed by the diffusion coefficients of oxygen in the oxide films.

(4) The substrate conditions (such as the number of defects) have a significant influence on the growth of the oxide film. Oxygen is prone to ingress FA-400 at the very beginning of the corrosion test since FA-400 is extrapolated to have the highest number of defects in the microstructure. In comparison, FA-400 has the lowest diffusion coefficient of oxygen in the oxide film. In terms of short-circuit diffusion and lattice diffusion, the lower diffusion coefficient of oxygen in the oxide film is caused by the lower fraction of short-circuit diffusion in the total diffusion. Therefore, it is speculated that fewer defects exist in the oxide film formed on FA-400 compared to the film formed on FA-450 and FA-500.

Author Contributions: Conceptualization, L.Z., L.-Y.C., and L.-C.Z.; Methodology, L.Z.; Software, L.Z. and Y.L.; Validation, L.Z.; Formal Analysis, L.Z. and C.Z.; Investigation, L.Z.; Resources, L.-Y.C.; Data Curation, L.Z.; Writing—Original Draft Preparation, L.Z.; Writing—Review & Editing, L.-C.Z.; Visualization, L.-C.Z.; Supervision, L.-C.Z.; Project Administration, L.-Y.C. and L.-C.Z.; Funding Acquisition, L.-Y.C.

Funding: The authors would like to acknowledge financial support provided by National Natural Science Foundation of China (51601075), China Postdoctoral Science Foundation Funded Project (2017M611751), open foundation of Guangxi Key Laboratory of Processing for Non-ferrous Metals and Featured Materials, Guangxi University (GXYSOF1801 and 2019GXYSOF01), and Jiangsu University of Science and Technology Overseas Research and Training Program for University Prominent Young and Middle-aged Teachers.

Conflicts of Interest: The authors declare no conflict of interest. The funders had no role in the design of the study; in the collection, analyses, or interpretation of data; in the writing of the manuscript; or in the decision to publish the results.

References

1. Yang, H.-Y.; Wang, Z.; Shu, S.-L.; Lu, J.-B. Effect of Ta addition on the microstructures and mechanical properties of in situ bi-phase (TiB_2-TiC_xN_y)/(Ni-Ta) cermets. *Ceram. Int.* **2019**, *45*, 4408–4417. [CrossRef]
2. Kudiiarov, N.V.; Larionov, V.V.; Tyurin, I.Y. Mechanical Property Testing of Hydrogenated Zirconium Irradiated with Electrons. *Metals* **2018**, *8*, 207. [CrossRef]
3. Yang, H.L.; Kano, S.; McGrady, J.; Shen, J.J.; Matsukawa, Y.; Chen, D.Y.; Murakami, K.; Abe, H. Surface orientation dependence of irradiation-induced hardening in a polycrystalline zirconium alloy. *Scr. Mater.* **2019**, *162*, 209–213. [CrossRef]
4. Chen, L.-Y.; Sang, P.; Zhang, L.; Song, D.; Chu, Y.-Q.; Chai, L.; Zhang, L.-C. Homogenization and growth behavior of second-phase particles in a deformed Zr–Sn-Nb-Fe-Cu-Si-O alloy. *Metals* **2018**, *8*, 759. [CrossRef]
5. Chen, L.; Li, J.; Zhang, Y.; Zhang, L.C.; Lu, W.; Zhang, L.; Wang, L.; Zhang, D. Effects of alloyed Si on the autoclave corrosion performance and periodic corrosion kinetics in Zr-Sn-Nb-Fe-O alloys. *Corros. Sci.* **2015**, *100*, 651–662. [CrossRef]
6. Chen, L.; Zeng, Q.; Li, J.; Lu, J.; Zhang, Y.; Zhang, L.-C.; Qin, X.; Lu, W.; Zhang, L.; Wang, L.; et al. Effect of microstructure on corrosion behavior of a Zr-Sn-Nb-Fe-Cu-O alloy. *Mater. Des.* **2016**, *92*, 888–896. [CrossRef]
7. Obrosov, A.; Sutygina, N.A.; Manakhov, A.; Bolz, S.; Weiß, S.; Kashkarov, B.E. Oxidation Behavior of Zr–1Nb Corroded in Air at 400 °C after Plasma Immersion Titanium Implantation. *Metals* **2018**, *8*, 27. [CrossRef]
8. Kashkarov, B.E.; Ryabchikov, I.A.; Kurochkin, V.A.; Syrtanov, S.M.; Shevelev, E.A.; Obrosov, A.; Weiß, S. Hydrogen Interaction with Deep Surface Modified Zr-1Nb Alloy by High Intensity Ti Ion Implantation. *Metals* **2018**, *8*, 1081. [CrossRef]

9. Lee, C.M.; Sohn, D.S. Enhanced high-temperature oxidation resistance of a zirconium alloy cladding by high-temperature preformed oxide on the cladding. *Corros. Sci.* **2018**, *131*, 116–125. [CrossRef]
10. Xie, S.; Zhou, B.; Liang, X.; Liu, W.; Li, H.; Li, Q.; Yao, M.; Zhang, J. A novel mechanism for nodular corrosion of Zircaloy-4 corroded in 773 K superheated steam. *Corros. Sci.* **2017**, *126*, 44–54. [CrossRef]
11. Huang, J.; Yao, M.; Chen, B.; Mao, Y.; Liang, X.; Zhang, J.; Zhou, B.; Li, Q. Oxidation behavior of Zr_9S_2 precipitates in Zr-0.8Sn-1.0Nb-0.3Fe-0.1Cr-xS alloys. *Corros. Sci.* **2017**, *120*, 82–89. [CrossRef]
12. Chen, L.Y.; Shen, P.; Zhang, L.; Lu, S.; Chai, L.; Yang, Z.; Zhang, L.C. Corrosion behavior of non-equilibrium Zr-Sn-Nb-Fe-Cu-O alloys in high-temperature 0.01 M LiOH aqueous solution and degradation of the surface oxide films. *Corros. Sci.* **2018**, *136*, 221–230. [CrossRef]
13. Wang, Z.; Zhou, B.X.; Pan, R.J.; Cao, X.X.; Wu, L.; Zhu, W.; Wen, B.; Fang, Z.Q.; Ovcharenko, Y.M.; He, W. Stress-driven grain re-orientation and merging behaviour found in oxidation of zirconium alloy using in-situ method and MD simulation. *Corros. Sci.* **2019**, *147*, 350–356. [CrossRef]
14. Qin, W. Improvement and Application of Zirconium Alloys. *Metals* **2018**, *8*, 794. [CrossRef]
15. Bakradze, G.; Jeurgens, L.P.H.; Acartürk, T.; Starke, U.; Mittemeijer, E.J.; Acartu, T. Atomic transport mechanisms in thin oxide films grown on zirconium by thermal oxidation, as-derived from 18 O-tracer experiments. *Acta Mater.* **2011**, *59*, 7498–7507. [CrossRef]
16. Abriata, J.P.; Garces, J.; Versaci, R. The O−Zr (oxygen-zirconium) system. *Bull. Alloy Phase Diagr.* **1986**, *7*, 116–124. [CrossRef]
17. Tapping, R.L. X-ray photoelectron and ultraviolet photoelectron studies of the oxidation and hydriding of zirconium. *J. Nucl. Mater.* **1982**, *107*, 151–158. [CrossRef]
18. Lyapin, A.; Jeurgens, L.P.H.; Mittemeijer, E.J. Effect of temperature on the initial, thermal oxidation of zirconium. *Acta Mater.* **2005**, *53*, 2925–2935. [CrossRef]
19. Zhang, J.; Hu, Y.; Huang, J.; Tu, L.; Yao, M.; Zhou, B. The corrosion resistance of Zr-0.7Sn-1Nb-0.2Fe-xCu-xGe alloys in 360 °C lithiated water. *Corros. Sci.* **2016**, *111*, 132–138. [CrossRef]
20. Kim, H.; Kim, I.; Choi, B.; Park, J.; Jeong, Y.; Kim, K. Study of the corrosion and microstructure with annealing conditions of a β-quenched HANA-4 alloy. *Corros. Sci.* **2010**, *52*, 3162–3167. [CrossRef]
21. Lee, J.H.; Hwang, S.K. Effect of Mo addition on the corrosion resistance of Zr-based alloy in water containing LiOH. *J. Nucl. Mater.* **2003**, *321*, 238–248. [CrossRef]
22. Park, J.Y.; Yoo, S.J.; Choi, B.K.; Jeong, Y.H. Oxide microstructures of advanced Zr alloys corroded in 360 °C water loop. *J. Alloys Compd.* **2007**, *437*, 274–279. [CrossRef]
23. Zhang, L.C.; Shen, Z.Q.; Xu, J. Mechanically milling-induced amorphization in Sn-containing Ti-based multicomponent alloy systems. *Mater. Sci. Eng. A* **2005**, *394*, 204–209. [CrossRef]
24. Liang, S.X.; Jia, Z.; Zhang, W.C.; Wang, W.M.; Zhang, L.C. Rapid malachite green degradation using Fe73.5Si13.5B9Cu1Nb3 metallic glass for activation of persulfate under UV–Vis light. *Mater. Des.* **2017**, *119*, 244–253. [CrossRef]
25. Zhang, L.C.; Xu, J.; Ma, E. Mechanically Alloyed Amorphous $Ti_{50}(Cu_{0.45}Ni_{0.55})_{44-x}Al_xSi_4B_2$ Alloys with Supercooled Liquid Region. *J. Mater. Res.* **2002**, *17*, 1743–1749. [CrossRef]
26. Zhang, L.C.; Kim, K.B.; Yu, P.; Zhang, W.Y.; Kunz, U.; Eckert, J. Amorphization in mechanically alloyed (Ti, Zr, Nb)-(Cu, Ni)-Al equiatomic alloys. *J. Alloys Compd.* **2007**, *428*, 157–163. [CrossRef]
27. Zhang, L.-C.; Chen, L.-Y. A review on biomedical titanium alloys: recent progress and prospect. *Adv. Eng. Mater.* **2019**, *21*, 1801215. [CrossRef]
28. Luan, B.F.; Chai, L.J.; Chen, J.W.; Zhang, M.; Liu, Q. Growth behavior study of second phase particles in a Zr-Sn-Nb-Fe-Cr-Cu alloy. *J. Nucl. Mater.* **2012**, *423*, 127–131. [CrossRef]
29. Chen, L.; Li, J.; Zhang, Y.; Lu, W.; Zhang, L.C.; Wang, L.; Zhang, D. Effect of low-temperature pre-deformation on precipitation behavior and microstructure of a Zr-Sn-Nb-Fe-Cu-O alloy during fabrication. *J. Nucl. Sci. Technol.* **2016**, *53*, 496–507. [CrossRef]
30. Chen, L.; Li, J.; Zhang, Y.; Zhang, L.; Lu, W.; Wang, L.; Zhang, L.-C.; Zhang, D. Zr-Sn-Nb-Fe-Si-O alloy for fuel cladding candidate: Processing, microstructure, corrosion resistance and tensile behavior. *Corros. Sci.* **2015**, *100*, 332–340. [CrossRef]
31. Yang, Z.N.; Wang, X.B.; Liu, F.; Zhang, F.C.; Chai, L.J.; Qiu, R.S.; Chen, L.Y. Effect of intercritical annealing temperature on microstructure and mechanical properties of duplex Zr-2.5Nb alloy. *J. Alloys Compd.* **2019**, *776*, 242–249. [CrossRef]

32. Zhang, M.; Li, Y.N.; Zhang, F.C.; Wang, X.B.; Chen, L.Y.; Yang, Z.N. Effect of annealing treatment on the microstructure and mechanical properties of a duplex Zr-2.5 Nb alloy. *Mater. Sci. Eng. A* **2017**, *706*, 236–241. [CrossRef]
33. Yang, H.; Shen, J.; Matsukawa, Y.; Satoh, Y.; Kano, S.; Zhao, Z.; Li, Y.; Li, F.; Abe, H. Effects of alloying elements (Sn, Nb, Cr, and Mo) on the microstructure and mechanical properties of zirconium alloys. *J. Nucl. Sci. Technol.* **2015**, *52*, 1162–1173. [CrossRef]
34. Cao, G.; Yun, Y.; Xu, H.; Yuan, G.; Hu, J.; Shao, G. A mechanism assessment for the anti-corrosion of zirconia coating under the condition of subcritical water corrosion. *Corros. Sci.* **2019**, *152*, 54–59. [CrossRef]
35. Almarshad, A.I.A.; Klein, A.C. A model for waterside oxidation of Zircaloy fuel cladding in pressurized water reactors. *J. Nucl. Mater.* **1991**, *183*, 186–194. [CrossRef]
36. Ishchenko, N.I. Determination of oxygen diffusion coefficient in oxide on zirconium alloys and adjacent metal from weight gain and oxide thickness measurement data. *Probl. At. Sci. Technol.* **2014**, *4*, 88–93.
37. Santamaria, M.; Di Franco, F.; Di Quarto, F.; Pisarek, M.; Zanna, S.; Marcus, P. Photoelectrochemical and XPS characterisation of oxide layers on 316L stainless steel grown in high-temperature water. *J. Solid State Electrochem.* **2015**, *19*, 3511–3519. [CrossRef]
38. Ma, X.; Toffolon-Masclet, C.; Guilbert, T.; Hamon, D.; Brachet, J.C. Oxidation kinetics and oxygen diffusion in low-tin Zircaloy-4 up to 1523 K. *J. Nucl. Mater.* **2008**, *377*, 359–369. [CrossRef]
39. García, E.A.; Kovacs, J. Diffusion model for the oxidation of zirconium at 573 and 623 K. *J. Nucl. Mater.* **1994**, *210*, 78–83. [CrossRef]
40. García, E.A. Dynamical diffusion model to simulate the oxide crystallization and grain growth during oxidation of zirconium at 573 and 623 K. *J. Nucl. Mater.* **1995**, *224*, 299–304. [CrossRef]
41. Yang, Y.; Yan, M.F.; Zhang, S.D.; Guo, J.H.; Jiang, S.S.; Li, D.Y. Diffusion behavior of carbon and its hardening effect on plasma carburized M50NiL steel: Influences of treatment temperature and duration. *Surf. Coat. Technol.* **2018**, *333*, 96–103. [CrossRef]
42. Yang, Z.; Chu, C.; Jiang, F.; Qin, Y.; Long, X.; Wang, S.; Chen, D.; Zhang, F. Accelerating nano-bainite transformation based on a new constructed microstructural predicting model. *Mater. Sci. Eng. A* **2019**, *748*, 16–20. [CrossRef]
43. Liang, S.X.; Jia, Z.; Zhang, W.C.; Li, X.F.; Wang, W.M.; Lin, H.C.; Zhang, L.C. Ultrafast activation efficiency of three peroxides by $Fe_{78}Si_9B_{13}$ metallic glass under photo-enhanced catalytic oxidation: A comparative study. *Appl. Catal. B Environ.* **2018**, *221*, 108–118. [CrossRef]
44. Chen, K.; Zeng, L.; Li, Z.; Chai, L.; Wang, Y.; Chen, L.-Y.; Yu, H. Effects of laser surface alloying with Cr on microstructure and hardness of commercial purity Zr. *J. Alloys Compd.* **2019**, *784*, 1106–1112. [CrossRef]
45. Chai, L.; Xia, J.; Zhi, Y.; Gou, Y.; Chen, L.; Yang, Z.; Guo, N. Deformation mode-determined misorientation and microstructural characteristics in rolled pure Zr sheet. *Sci. China Technol. Sci.* **2018**, *61*, 1346–1352. [CrossRef]
46. Wang, L.; Xie, L.; Lv, Y.; Zhang, L.-C.; Chen, L.; Meng, Q.; Qu, J.; Zhang, D.; Lu, W. Microstructure evolution and superelastic behavior in Ti-35Nb-2Ta-3Zr alloy processed by friction stir processing. *Acta Mater.* **2017**, *131*, 499–510. [CrossRef]
47. Su, L.H.; Lu, C.; He, L.Z.; Zhang, L.C.; Guagliardo, P.; Tieu, A.K.; Samarin, S.N.; Williams, J.F.; Li, H.J. Study of vacancy-type defects by positron annihilation in ultrafine-grained aluminum severely deformed at room and cryogenic temperatures. *Acta Mater.* **2012**, *60*, 4218–4228. [CrossRef]
48. Calin, M.; Zhang, L.C.; Eckert, J. Tailoring of microstructure and mechanical properties of a Ti-based bulk metallic glass-forming alloy. *Scr. Mater.* **2007**, *57*, 1101–1104. [CrossRef]
49. Zhu, K.Y.; Chaubet, D.; Bacroix, B.; Brisset, F. A study of recovery and primary recrystallization mechanisms in a Zr-2Hf alloy. *Acta Mater.* **2005**, *53*, 5131–5140. [CrossRef]
50. Dong, B.-X.; Yang, H.-Y.; Qiu, F.; Li, Q.; Shu, S.-L.; Zhang, B.-Q.; Jiang, Q.-C. Design of TiC nanoparticles and their morphology manipulating mechanisms by stoichiometric ratios: Experiment and first-principle calculation. *Mater. Des.* **2019**, *181*, 107951. [CrossRef]
51. Yang, H.L.; Kano, S.; Matsukawa, Y.; Li, Y.F.; Shen, J.J.; Zhao, Z.S.; Li, F.; Satoh, Y.; Abe, H. Study on recrystallization and correlated mechanical properties in Mo-modified Zr-Nb alloys. *Mater. Sci. Eng. A* **2016**, *661*, 9–18. [CrossRef]
52. Gong, W.; Zhang, H.; Qiao, Y.; Tian, H.; Ni, X.; Li, Z.; Wang, X. Grain morphology and crystal structure of pre-transition oxides formed on Zircaloy-4. *Corros. Sci.* **2013**, *74*, 323–331. [CrossRef]

53. Garner, A.; Preuss, M.; Frankel, P. A method for accurate texture determination of thin oxide films by glancing-angle laboratory X-ray diffraction. *J. Appl. Crystallogr.* **2014**, *47*, 575–583. [CrossRef]
54. Wei, J.; Frankel, P.; Polatidis, E.; Blat, M.; Ambard, A.; Comstock, R.J.; Hallstadius, L.; Hudson, D.; Smith, G.D.W.; Grovenor, C.R.M.; et al. The effect of Sn on autoclave corrosion performance and corrosion mechanisms in Zr-Sn-Nb alloys. *Acta Mater.* **2013**, *61*, 4200–4214. [CrossRef]
55. Vermaak, N.; Parry, G.; Estevez, R.; Bréchet, Y. New insight into crack formation during corrosion of zirconium-based metal-oxide systems. *Acta Mater.* **2013**, *61*, 4374–4383. [CrossRef]
56. Parise, M.; Sicardy, O.; Cailletaud, G. Modelling of the mechanical behavior of the metal–oxide system during Zr alloy oxidation. *J. Nucl. Mater.* **1998**, *256*, 35–46. [CrossRef]
57. Chai, L.; Wang, T.; Ren, Y.; Song, B.; Guo, N.; Chen, L. Microstructural and Textural Differences Induced by Water and Furnace Cooling in Commercially Pure Zr Annealed in the α + β Region. *Met. Mater. Int.* **2018**, *24*, 673–680. [CrossRef]
58. Chen, L.-Y.; Wang, H.; Zhao, C.; Lu, S.; Wang, Z.-X.; Sha, J.; Chen, S.; Zhang, L.-C. Automatic remelting and enhanced mechanical performance of a plasma sprayed NiCrBSi coating. *Surf. Coat. Technol.* **2019**, *369*, 31–43. [CrossRef]
59. Liu, L.H.; Yang, C.; Wang, F.; Qu, S.G.; Li, X.Q.; Zhang, W.W.; Li, Y.Y.; Zhang, L.C. Ultrafine grained Ti-based composites with ultrahigh strength and ductility achieved by equiaxing microstructure. *Mater. Des.* **2015**, *79*, 1–5. [CrossRef]
60. Chen, L.Y.; Xu, T.; Lu, S.; Wang, Z.X.; Chen, S.; Zhang, L.C. Improved hardness and wear resistance of plasma sprayed nanostructured NiCrBSi coating via short-time heat treatment. *Surf. Coat. Technol.* **2018**, *350*, 436–444. [CrossRef]
61. Li, C.-L.; Qiu, F.; Chang, F.; Zhao, X.-M.; Geng, R.; Yang, H.-Y.; Zhao, Q.-L.; Jiang, Q.-C. Simultaneously Enhanced Strength, Toughness and Ductility of Cast 40Cr Steels Strengthened by Trace Biphase TiCx-TiB2 Nanoparticles. *Metals* **2018**, *8*, 707. [CrossRef]
62. Zhang, L.-C.; Liang, S.-X. Fe-based Metallic Glasses in Functional Catalytic Applications. *Chem. Asian J.* **2018**, *13*, 3575–3592. [CrossRef]
63. Li, Q.; Qiu, F.; Gao, Y.-Y.; Dong, B.-X.; Shu, S.-L.; Lv, M.-M.; Yang, H.-Y.; Zhao, Q.-L.; Jiang, Q.-C. Microstructure refinement and strengthening mechanisms of bimodal-sized and dual-phased (TiCn-Al_3Tim)/Al hybrid composites assisted ultrasonic vibration. *J. Alloys Compd.* **2019**, *788*, 1309–1321. [CrossRef]
64. Liang, S.X.; Jia, Z.; Liu, Y.J.; Zhang, W.; Wang, W.; Lu, J.; Zhang, L.C. Compelling Rejuvenated Catalytic Performance in Metallic Glasses. *Adv. Mater.* **2018**, *30*, 1802764. [CrossRef]
65. Zhang, L.C.; Jia, Z.; Lyu, F.; Liang, S.X.; Lu, J. A review of catalytic performance of metallic glasses in wastewater treatment: Recent progress and prospects. *Prog. Mater. Sci.* **2019**, *105*, 100576. [CrossRef]
66. Panicaud, B.; Retraint, D.; Grosseau-Poussard, J.-L.; Li, L.; Guérain, M.; Goudeau, P.; Tamura, N.; Kunz, M. Experimental and numerical study of the effects of a nanocrystallisation treatment on high-temperature oxidation of a zirconium alloy. *Corros. Sci.* **2012**, *60*, 224–230. [CrossRef]
67. Wang, Z.; Zhou, B.X.; Chen, B.; Zhu, W.; Wen, B.; Wu, L.; Tang, H.K.; Fang, Z.Q.; Li, Q.; Yao, M. In-situ oxidation and short-time corrosion investigation on strain and dislocation during the generation and growth of ZrO_2. *Corros. Sci.* **2017**, *122*, 26–31. [CrossRef]
68. Smeltzer, W.W.; Haering, R.R.; Kirkaldy, J.S. Oxidation of metals by short circuit and lattice diffusion of oxygen. *Acta Metall.* **1961**, *9*, 880–885. [CrossRef]
69. Ly, A.; Ambard, A.; Blat-Yrieix, M.; Legras, L.; Frankel, P.; Preuss, M.; Curfs, C.; Parry, G.; Brechet, Y.; Barberis, P.; et al. Understanding Crack Formation at the Metal/Oxide Interface During Corrosion of Zircaloy-4 Using a Simple Mechanical Model. *J. ASTM Int.* **2011**, *8*, 103550. [CrossRef]
70. Liu, Y.Z.; Park, J.Y.; Kim, H.G.; Jeong, Y.H. Oxide structure and corrosion mechanism of ZrSnNbFeCrCu alloy studied with transmission electron microscopy and nano-indentation: Relation to corrosion kinetics. *Mater. Chem. Phys.* **2010**, *122*, 408–416. [CrossRef]
71. Kim, H.G.; Choi, B.K.; Park, J.Y.; Jeong, Y.H. Influence of the manufacturing processes on the corrosion of Zr-1.1Nb-0.05Cu alloy. *Corros. Sci.* **2009**, *51*, 2400–2405. [CrossRef]